energies

MDPI

Article

Development and Validation of a Transient Electro-Thermo-Mechanical Model for Parabolic Dish Micro Gas Turbines

Shahrbanoo Shamekhi Amiri [1], Jafar Al-Zaili [1,*] and Abdulnaser I. Sayma [2]

[1] Department of Engineering, School of Science and Technology, City St George's University of London, Northampton Square, London EC1V 0HB, UK; shahrbanoo.shamekhi-amiri.2@citystgeorges.ac.uk
[2] College of Engineering, Design and Physical Sciences, Brunel University of London, Kingston Lane, London UB8 3PH, UK; abdulnaser.sayma@brunel.ac.uk
* Correspondence: jafar.alzaili@city.ac.uk

Abstract

Small-scale concentrated solar power (CSP) systems coupled with micro gas turbines (MGTs) offer a promising solution for decentralised and sustainable power generation. However, CSP–MGT systems are subject to pronounced transient behaviour during start-up and operation due to fluctuating solar irradiance, making accurate transient modelling essential. This work introduces a fully coupled transient electro-thermo-mechanical model of a CSP-driven micro gas turbine, explicitly linking thermal transients and heat soakage effects to electrical performance during start-up. Unlike existing models, the proposed approach captures the interaction between turbomachinery thermal inertia, shaft dynamics, and detailed electrical machine and power converter losses under real-world transient operating conditions. The model integrates thermodynamic, mechanical, electrical, and control subsystems within a unified framework using a lumped-volume formulation suitable for real-time-capable simulations. To improve prediction accuracy at low rotational speeds, a dedicated interpolation strategy for turbomachinery performance maps is implemented. The model is validated at both component and system levels using experimental data from a 6 kWe CSP–MGT test facility. The results show good agreement with measurements, with maximum deviations of approximately 8% in receiver outlet temperature and less than 6% in air mass flow rate. The findings demonstrate that accounting for heat soakage is critical for a realistic prediction of thermal and electrical transients, as neglecting thermal inertia leads to an underestimation of the start-up electrical energy consumption by up to 140%, highlighting the dominant role of thermal mass effects in small-scale micro gas turbines compared to larger systems. The proposed model provides a robust tool for analysing start-up behaviour and supports improved control and operational strategy development for CSP–MGT systems under variable solar conditions.

Keywords: micro gas turbine; concentrated solar power system; transient modelling; electro-thermo-mechanical model; start-up phase; heat soakage

Received: 4 January 2026
Revised: 5 February 2026
Accepted: 8 February 2026
Published: 27 February 2026

1. Introduction

In response to climate change and population growth, there has been a global surge in the transition to renewable energy. This is mainly for limiting the global temperature increase to 1.5 °C, which is required for the global net-zero CO_2 emissions aim, by 2050 [1]. Furthermore, the challenge of global electricity access, emphasises the importance of distributed generation and reducing centralised power generation in developed nations' energy sectors [2–4].

Solar power, as one of the most important renewable energy resources, can be harnessed through photovoltaic (PV) and concentrated solar power (CSP) technologies [5,6]. CSP technology can supply process heat at temperatures of up to 1500 °C [7]. Therefore, CSP systems with efficient thermodynamic engines, offer high efficiency and power density, making them suitable for distributed power generation in regions with high Direct Nominal Irradiance (DNI) [8]. Additionally, CSP systems can provide on-demand power due to their integration with thermal energy storage and hybridisation with other renewable fuels [9].

Therefore, the integration of solar CSP with gas turbines as a thermodynamic engine has been mostly investigated in hybrid configurations [10–13]. Regardless of the configuration, evaluating the transient performance of the gas turbine is crucial for reliable operation, especially in a solar-powered system. Factors like load variations, environmental shifts, and start-up/shutdown processes contribute to transient events, particularly in CSP-MGT systems where these transient behaviours can be more significant [14,15]. Reliability concerns include compressor surges and solar receiver thermal safety [16]. Therefore, sophisticated and accurate mathematical models are essential for investigating the reliability of the system, optimal parameter definitions, and enhancing components design [17–19].

Gas turbine transient modelling began in the 1950s with twin-spool engines [20]. Kim et al. [21] developed a model for recuperated natural gas-fuelled MGTs, which lacked volume dynamics and heat soakage considerations. Traverso [22] addressed these gaps in the Transeo model, which made the model suitable for modelling the MGT for all operating modes including start-up, generation and shutdown. Considering volume dynamics causes delays in MGT response, leading to two methodologies: iterative constant mass flow (ICMF) and inter-component volume (ICV) [23,24]. On the one hand, ICV allows pressure variations before large volumes like recuperators and is preferred for smoother operation in turbomachinery performance maps [25,26]. It offers precise transient representation, which is beneficial in control design. ICV is preferred in real-time simulations for faster computation, despite the capabilities of the full dynamic model [27]. On the other hand, ICMF includes complex iterative calculations for mass continuity equations and limited real-time applicability [28].

Transient modelling of gas turbine systems, especially during start-up, must consider thermal transients or heat soakage, where heat accumulates inside the metal of the components of the system. This feature is not taken into account in off-design models [17]. Kim et al. [29] studied this in a large gas turbine start-up, finding 8.3% of fuel energy absorbed by metal due to heat soakage. While large gas turbines are less affected by thermal effects, MGTs are significantly impacted due to their more compact design, necessitating the consideration of heat soakage, especially during start-up analysis where temperature differences are significant.

Start-up analyses for gas turbines often overlook crucial early stages for assessing compressor safety and estimating starter capacity. Studying the transient behaviour from standstill (zero speed) requires compressor and turbine maps, which are usually unavailable for low speeds. Generating such maps involves complex extrapolation methods [29] which are prone to unreliability [30]. Efforts have been made to enhance the accuracy of generated maps at the low-speed range including virtual zero-speed lines [31], locked rotor compressor experimental tests [32], and CFD methods [33,34]. However, for turbines, introducing a zero-speed line may cause non-matching issues which were resolved by introducing a zero point [35].

In addition to the mentioned challenges, it is worth noting that many existing transient models for MGTs in the literature belong to the fuelled ones or hybrid configurations where input thermal power is controlled by altering the fuel flow rate [36–39]. Nonetheless, no research has been conducted regarding the development of a transient model for a CSP-

MGT system where there is no controllable input of thermal power. Apart from that, most of the studies predominantly focus on the thermo-mechanical aspects, giving less attention to the electrical component. Typically, they only incorporate electrical efficiency without delving into a detailed electrical system model that factors in power loss, dependent on voltage and current.

In CSP-MGTs, understanding electric current values during start-up and acceleration is critical due to the established drive plausibility limits on this parameter. Additionally, it is essential to track the voltage of the permanent magnet synchronous machine (PMSM), a primary speed control parameter. Consequently, this research aims to develop a comprehensive transient model capable of encompassing the thermodynamic, mechanical, and electrical parts of CSP-MGTs, with a specific focus on the start-up phase, although it has potential applications in other operational modes as well. Afterwards, it will be validated against measurements obtained from the project of an Optimised Microturbine Solar Power system (OMSoP).

2. General Model Description

The CSP-MGT cycle comprises four key components: a compressor, a heat source (e.g., combustion chamber or solar receiver), a turbine, and a recuperator (shown in Figure 1). Furthermore, there is a high-speed alternator (HSA), capable of transforming mechanical power into electrical power or operating as a motor during start-up. In CSP-MGT, the compressor pressurises air to receive thermal energy from a heat source. After receiving thermal energy, the air is of high temperature and high pressure. Afterwards, the hot air passes through the turbine, expanding and generating mechanical work before exiting to the recuperator, where a proportion of waste heat is transferred to the incoming compressor air, enhancing the thermal efficiency of the cycle.

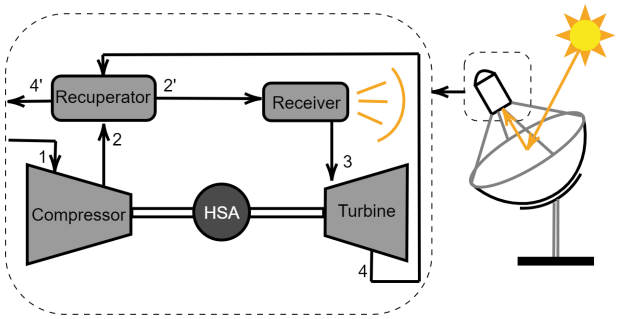

Figure 1. Schematic of a CSP-MGT system. (1) compressor inlet, (2) compressor outlet, (3) turbine inlet, (4) turbine outlet, (2′) recuperator outlet and receiver inlet, (4′) recuperator outlet.

A lumped-volume approach is used for the CSP-MGT transient model, making simulation speed suitable for real-time applications. Having a zero-dimensional model for each component, the recuperator and solar receiver are modelled by a one-dimensional approach to consider the volumetric and thermal capacitance effects within the components. Mass, momentum, and energy conservation equations are solved for each component. Implemented in MATLAB/Simulink, this model comprises three system-level parts: the thermodynamic, electrical, and control system models. The first two are interconnected through a mechanical interface within the rotating shaft (thermo-mechanical model), dealing with mechanical and electric torque, losses, and rotational speed alterations. The governing equations of each component are explained in the following paragraphs.

Modelling assumptions that are used throughout the modelling procedure are as follows:

(a) Air is modelled as a semi-ideal gas that adheres to the ideal gas law while allowing its thermo-physical properties to vary with temperature.

(b) Thermodynamic effects within the pipes and connections, including pressure drops and heat losses, are neglected in this analysis.

(c) Conductive heat transfer within the metal components is neglected due to the dominance of convective heat transfer, which is significantly higher in magnitude.

(d) Flow leakage is assumed to be negligible due to the presence of effective sealing.

(e) Natural convection heat losses in the compressor, turbine, and recuperator are neglected due to insulation.

3. Thermo-Mechanical Model

The thermo-mechanical model comprises the following key components: a centrifugal compressor, radial turbine, recuperator, solar receiver, shaft and plenum (artificial component). The operating conditions of the components are determined through performance maps or conservation laws. Detailed governing equations for each component are explained in this section.

3.1. Turbomachinery Components Models

The compressor and turbine model follows a sequentially structured thermal modelling approach, consisting of two distinct segments. The first segment employs a zero-dimensional quasi-steady-state approach to determine operating points based on steady-state performance maps [40]. The second segment incorporates a lumped-volume method to capture thermal transients and their influence on airflow temperatures [29]. Furthermore, to enhance the accuracy of performance maps at low rotational speeds, interpolation techniques are applied, introducing a zero-speed reference point for the turbine and a zero-speed characteristic curve for the compressor [35].

3.1.1. Compressor Model

The operating point of the MGT on the compressor map is found by linear interpolation in the performance maps. By using the pressure ratio and isentropic efficiency from the performance map, the steady-state outlet air temperature of the compressor is calculated:

$$T_{2,ss} = T_1\left(1 + \frac{1}{\eta_c}\left[\pi_c{}^{\frac{\gamma-1}{\gamma}} - 1\right]\right) \tag{1}$$

where $T_{2,ss}$, T_1, η_c, π_c and γ are the steady-state compressor outlet air temperature, inlet temperature of the compressor, compressor isentropic efficiency, compressor pressure ratio and specific heat ratio. The subscripts of 1, 2, $2,ss$ and c present the compressor inlet, compressor outlet, steady-state compressor outlet and compressor. The power requirement of the compressor is calculated by the steady-state outlet air of the compressor:

$$PW_c = \dot{m}_c c_{p,c}(T_{2,ss} - T_1) \tag{2}$$

where PW_c and c_p are the required power by the compressor and specific heat.

For the second segment of the compressor model, the energy conservation equations related to the heat soakage in compressor metal are solved for an equivalent duct. To calculate the heat transfer coefficient, the Dittus–Boelter correlation for the Nusselt number is used [41]. The Dittus–Boelter correlation was employed for heat transfer calculations in the compressor and later on in the turbine because the present model is a lumped, system-level transient simulation rather than a blade-resolved aerodynamic model. Under normal MGT operating conditions, the internal flows in compressor and turbine passages

are fully turbulent and characterised by high Reynolds numbers, making classical turbulent forced-convection correlations appropriate. This modelling approach is consistent with the established literature on transient micro gas turbine simulations, where simplified Nusselt number correlations are commonly used to represent average gas-casing heat transfer while detailed aerodynamic effects are captured through component performance maps rather than local heat transfer models. Similar assumptions and correlation-based heat transfer formulations are adopted, for example, by Henke et al. in their validated DLR micro gas turbine cycle simulation framework [42]. The heat transfer between compressor metal and air is calculated as follows:

$$Q_{m,c} = h_c A_c (T_{a,c} - T_{m,c}) \tag{3}$$

$$Nu_c = 0.023 Re_c^{0.8} Pr_c^{0.33} \tag{4}$$

$$h_c = \frac{Nu_c k_{air}}{D_c} \tag{5}$$

where $Q_{m,c}$, h_c, A_c, Nu_c, Re_c, Pr_c, k_{air} and D_c are heat transfer rate, convective heat transfer coefficient, heat transfer area, Nusselt, Reynolds and Prantdl number, thermal conductivity of air and hydraulic diameter of the equivalent duct of the compressor and the subscripts of m, c and a, c refer to the mean-wall of the compressor and air as the compressor working fluid. The temperature of $T_{a,c}$ which is the inside air of the compressor is calculated by getting an average between the inlet and outlet temperature of the compressor ($(T_1 + T_2)/2$). This results in a different compressor outlet temperature. As shown in Equation (7), the heat transfer rate which is delivered to or taken from the compressor working fluid is the difference of the heat transfer rate from the required power of the compressor:

$$Q_{m,c} = M_c C_c \frac{dT_{m,c}}{dt} \tag{6}$$

$$T_2 = T_{2,ss} - \frac{PW_c - Q_{m,c}}{\dot{m}_c c_p} \tag{7}$$

where M_c and C_c represent compressor metal mass and specific heat capacity. This equation implies that the work done to compress the air is independent of the heat transfer between the air and the metal. The reason is that the air has already received its compression power before transferring heat to the metal.

3.1.2. Turbine Model

The modelling procedure of the turbine is similar to the compressor using a two-segment strategy. The steady-state outlet temperature of the turbine is computed as follows:

$$T_{4,ss} = T_3 \left(1 + \eta_t \left[\left(\frac{1}{\pi_t} \right)^{\frac{\gamma-1}{\gamma}} - 1 \right] \right) \tag{8}$$

where T_3, $T_{4,ss}$, η_c, π_c are the steady-state turbine inlet air temperature, outlet air temperature, turbine isentropic efficiency and turbine pressure ratio. The subscripts of 3, 4, 4, ss and t subscripts account for the inlet air of the turbine, outlet air of the turbine, steady-state outlet of the turbine and the turbine. The governing equations of the second segment of the turbine model are written below:

$$Q_{m,t} = h_t A_t (T_{a,t} - T_{m,t}) \tag{9}$$

$$Q_{m,t} = M_t C_t \frac{dT_{m,t}}{dt} \tag{10}$$

where $Q_{m,t}$, h_t, A_t are turbine heat transfer rate, convective heat transfer coefficient, heat transfer area, and the subscripts of m,t and a,t refer to the mean-wall of the turbine and air as the turbine working fluid. The convective heat transfer coefficient (h_t) of the second segment is found using the same correlation that was used for the compressor. The temperature of $T_{a,t}$ as the inside air of the turbine is calculated with a similar strategy to the compressor. The generated power of the turbine in case of not considering the heat soakage ($PW_{t,ss}$) is calculated as follows:

$$PW_{t,ss} = \dot{m}_t c_{p,t}(T_3 - T_{4,ss}) \tag{11}$$

Consequently, the final generated power that includes heat soakage is found with the help of the following equation:

$$PW_t = PW_{t,ss} - Q_{m,t} \tag{12}$$

This means that the generated power of the turbine considering the heat soakage is less than the case where no heat transfer is taken into account. The outlet temperature of the turbine is therefore calculated by using the actual generated power:

$$T_4 = T_{4,ss} - \frac{Q_{m,t}}{\dot{m}_t c_{p,t}} \tag{13}$$

where T_4 is the turbine outlet temperature by considering the heat soakage.

3.2. Recuperator Model

The recuperator is modelled as a counterflow heat exchanger with 1D approach, divided into unit volumes using lumped-volume approximations, as seen in Figure 2.

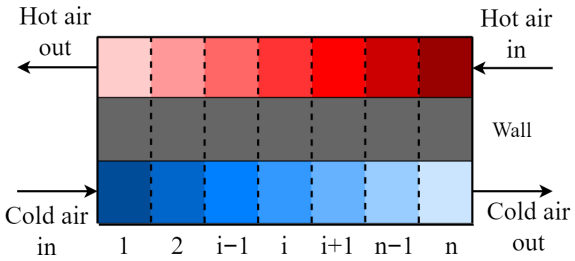

Figure 2. Thermal modelling approach of the recuperator.

Energy conservation is applied for each cell of the recuperator wall with Equation (14). The energy conservation for fluid cells in both cold and hot sides is seen in Equations (15) and (16).

$$\begin{aligned} \frac{M_{recu}C_{recu}}{n}\frac{dT_i^{m,recu}}{dt} =& \dot{m}_{hot}c_{p,hot}\left(T_i^{hot} - T_{i+1}{}^{hot}\right) - \\ & \dot{m}_{cold}c_{p,cold}\left(T_{i+1}{}^{cold} - T_i^{cold}\right) \end{aligned} \tag{14}$$

where M_{recu}, C_{recu}, $\dot{m}_{hot}$, $\dot{m}_{cold}$, $c_{p,hot}$ and $c_{p,cold}$ are recuperator wall mass, recuperator wall specific heat capacity, hot- and cold-side air mass flow rates, and hot- and cold-side air specific heat capacity. The temperatures of $T_i^{m,recu}$, T_i^{hot} and T_i^{cold} are the mean-wall temperatures of the recuperator metal and the hot-side and cold-side air temperature for cell of number i. The parameter of n refers to the number of cells and the subscript of i accounts for the particular cell number. The energy conservation equations for the hot- and cold-side air are shown in Equations (15) and (16).

$$\dot{m}_{hot} c_{p,hot} \left({T_i}^{hot} - {T_{i+1}}^{hot} \right) = \frac{h_{hot} A_{hot}}{n} \left(\frac{{T_i}^{hot} + {T_{i+1}}^{hot}}{2} - {T_i}^{m,recu} \right) \quad (15)$$

$$\dot{m}_{cold} c_{p,cold} \left({T_{i+1}}^{cold} - {T_i}^{cold} \right) = \frac{h_{cold} A_{cold}}{n} \left({T_i}^{m,recu} - \frac{{T_i}^{cold} + {T_{i+1}}^{cold}}{2} \right) \quad (16)$$

This computation includes the difference between the average wall temperature of the recuperator at cell index i and the average temperature of the incoming and outgoing airflow, denoted by subscripts i and $i+1$. The heat transfer areas (A_{hot} and A_{cold}) and coefficients of the hot (h_{cold}) and cold sides (h_{hot}) are determined using the geometric details of a heat exchanger with similar performance parameters from [43]. The selected heat exchanger is a plate-fin heat exchanger that is an offset strip fin type. The heat transfer coefficient in this type of heat exchanger is found by the below equation which is shown for fluid 1 developed by Manglik and Bergles [44]:

$$h_1 = \frac{j_1 G_1 cp_1}{Pr_1^{2/3}} \quad (17)$$

where j is Colburn number [44] which is defined as the ratio of the convective heat transfer coefficient to the product of the fluid's heat capacity and its velocity. G is fluid mass velocity based on the minimum free-flow area ($\dot{m}/A_1$) where A_1 is the cross-section of fluid 1.

The pressure drop for a plate-fin heat exchanger on both sides is found with Equation (18) [45]:

$$\Delta p_{recu} = \frac{4fLG^2}{2D_h} \frac{1}{\rho_m} \quad (18)$$

where f, L, D_h and ρ_m are the fanning friction factor, airflow length on one side of the heat exchanger, hydraulic diameter, and the average of inlet and outlet fluid density, respectively. The term of $(1/\rho)_m$ is calculated by $(1/\rho_{in} + 1/\rho_{out})$ where ρ_{in} and ρ_{out} refer to the inlet and outlet air of one side of the recuperator.

3.3. Concentrated Solar Power Dish and Solar Receiver Models

The solar parabolic dish is defined by an optical efficiency (η_{opt}) which is the ratio between the thermal power entering the receiver window and the power intercepted on the mirror surface. The solar receiver, functioning as a heat exchanger like the recuperator, utilises an impinging cavity design in this study [46] due to efficient heat transfer from the impinging jet [47], assuming uniform heat transfer coefficients and wall temperatures along the air flow is impractical [48]. Therefore, a one-dimensional modelling approach, maintaining uniform cell temperatures around the cavity receiver perimeter, is more reasonable. Figure 3 illustrates the one-dimensional receiver modelling approach.

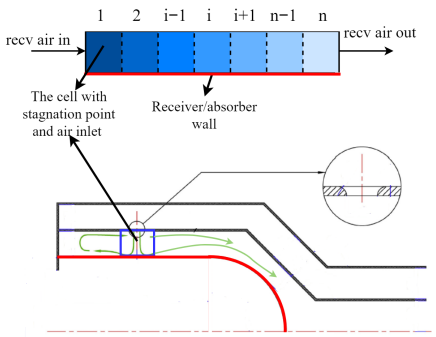

Figure 3. Thermal modelling approach of the solar receiver.

The schematic in Figure 3 depicts the fluid path (green arrows) and the receiver/absorber wall (red line), divided into n cells. The first cell (blue square) contains the stagnation point from the impinging jet, where high-velocity fluid meets the surface, creating zero velocity and increased pressure. Cells 2 to n follow the flow path towards the air outlet, starting from the left side of the jet and then the right. Each cell acts as a lumped volume, addressing conservation equations for energy in the receiver's metal. The governing equation for a single cell is expressed below:

$$\frac{1}{n}Q_{in} - \frac{1}{n}Q_{loss} - Q_{abs,i} = \frac{1}{n}M_{recv}C_{recv}\frac{dT_{m,recv,i}}{dt} \tag{19}$$

where the subscripts of $in, loss, abs, i, recv$ and $m, recv, i$ refer to the input heat to the solar receiver, heat loss, absorbed heat by the air inside the ith cell, the receiver and mean-wall of the receiver. All values of the heat transfer rates of Equation (19) are found below.

The intercepted heat on the cavity receiver wall is calculated based in the below equation:

$$Q_{in} = DNIA_{eff}\eta_{opt} \tag{20}$$

where A_{eff} is the effective area of the solar parabolic dish.

Heat loss of the solar receiver mainly accounts for two main losses, convection and radiation heat loss, which are calculated with the below equations. The heat transfer coefficients are found based on the equations provided in [49].

$$Q_{loss} = Q_{conv,loss} + Q_{rad,loss} \tag{21}$$

$$Q_{conv,loss} = h_{conv,loss}A_{recv}(T_{m,recv} - T_{amb}) \tag{22}$$

$$Q_{rad,loss} = U_{rad,loss}A_{recv}(T_{m,recv} - T_{amb}) \tag{23}$$

where U is the radiative heat transfer coefficient and the subscripts of $conv, loss, rad, loss, amb, m, recv$ refer to convection loss, radiation loss, ambient condition and mean-wall of the receiver.

The absorbed heat by the air for each cell is attributed to the heat transfer coefficient and the heat transfer area between the air and the absorber wall in that specific cell:

$$Q_{abs,i} = h_{abs,i}A_{recv}\left(T_{m,recv,i} - \frac{T_{recv,in,i} + T_{recv,out,i}}{2}\right) \tag{24}$$

in which the subscripts of $abs, i, recv, in, i$ and $recv, out, i$ refer to absorbed heat by air in the ith cell, the receiver inlet and outlet air associated with the ith cell.

The heat transfer coefficient in each cell is calculated differently depending on the distance from the stagnation point. The local heat transfer coefficient for the cells that are affected by the impinging jet, is calculated as follows [50]:

$$Nu_x = 0.055{Re_{st}}^{0.75}Pr^{0.42}e^{-0.025(x/d)^2} \quad 0 \le x/d \le 8 \tag{25}$$

$$h_x = \frac{Nu_x k_{air}}{d} \tag{26}$$

$$Re_{st} = \frac{4\dot{m}}{\mu n_{nozzle}\pi d} \tag{27}$$

where x, d, k_{air} and n_{nozzle} are the distance from the stagnation point, nozzle diameter, air thermal conductivity and the number of nozzles on the receiver. The subscripts of x and st are referred to as the distance from the stagnation point to represent the local parameter and stagnation point. This equation is only valid for a limited distance from the stagnation point. For the cells, where x/d is higher than the value of 8, the heat transfer coefficient is

calculated by using the Dittus–Boelter Nusselt empirical correlation [41]. Since the flow is in the fully turbulent regime and the flow path length is sufficiently large compared to the characteristic diameter, the use of the Dittus–Boelter correlation is appropriate. Although the overall mass flow rate can be low, the local Reynolds number based on the jet diameter remains high due to the small nozzle size, resulting in fully turbulent flow. Consequently, the heat transfer coefficients are not highly sensitive to small variations in mass flow rate.

$$Nu = 0.023 Re^{0.8} Pr^{0.33} \tag{28}$$

The main pressure drop in the receiver is attributed to the jet impingement on the absorber wall. Therefore, it is reasonable to compute the pressure drop by computing the maximum existing pressure drop [48,51]:

$$\Delta p_{recv} = \frac{\rho {V_{jet}}^2}{2{C_d}^2} \tag{29}$$

in which ρ, C_d are jet air density, discharge coefficient and V_{jet} is the air jet velocity that is calculated as

$$V_{jet} = \frac{4\dot{m}}{n_{nozzle}\pi\rho d^2} \tag{30}$$

where n_{nozzle} and d are the total nozzle number in the receiver geometry and the diameter of the nozzle exit hole.

3.4. Plenum Model

The plenum is an artificial component that has been added to the thermodynamic model to take into account mass imbalances which are implemented by solving the mass conservation equation. To account for this effect, an equation is formulated to describe the change in compressor outlet pressure associated with the inlet and outlet mass flow rates which are found using the compressor and turbine performance maps, as discussed earlier:

$$\frac{dp_2}{dt} = \frac{RT_2}{V_{plenum}}(\dot{m}_c - \dot{m}_t) \tag{31}$$

where R and V_{plenum} represent the gas constant and the plenum volume, respectively. The plenum volume is a combination of the air side volumes of the cold side of the recuperator and solar receiver.

Shaft Model

The shaft is the component that represents the mechanical model of the system. It undergoes four main sources of torque: Compressor, turbine, PMSM and torque losses. Therefore, by writing the energy conservation for the MGT shaft, the differential equation of the shaft is given by

$$\tau_t - \tau_c - \tau_A - \tau_{loss} = J\frac{d\omega}{dt} \tag{32}$$

where τ, ω and J are torque in $N.m.$, rotational speed in rad/s and shaft inertia, and the subscripts of t, c, A and $loss$ refer to the turbine, compressor, high-speed alternator (PMSM) and mechanical loss. The compressor and turbine torques for each time step are calculated as follows:

$$\tau_c = \frac{PW_c}{\omega} \tag{33}$$

$$\tau_t = \frac{PW_t}{\omega} \tag{34}$$

The torque loss is linked to the power reduction caused by the presence of bearings along the shaft. The power loss of the shaft called mechanical loss is calculated as follows for one bearing [30] and will be multiplied by the number of bearings on the shaft:

$$PW_{loss} = 4.87 \times 10^{-15} D^{3.95} N^{1.75} \mu_{oil}^{0.4} + 3.19 \times 10^{-10} N D \dot{m}_{oil} \quad (35)$$

where D, μ_{oil} and $\dot{m}_{oil}$ are pitch circle diameter of the bearing, oil viscosity and oil mass flow rate. The value of the oil mass flow rate is assumed to be constant in this study. By dividing the power loss over rotational speed, the torque loss is calculated.

4. Electric Model

In the CSP-MGT system, the electrical components play a crucial role in converting mechanical to electrical power and electrical to mechanical power. These components operate in both modes of generation and motoring, with a focus on the latter during start-up. The CSP-MGT electrical system includes three main elements: a PMSM as the high-speed alternator, grid-side or load-side bi-directional converter, and PMSM-side bi-directional converter (see Figure 4). These converters can perform AC/DC and DC/AC transformations. During motoring mode in a grid-connected system, the grid-side converter converts three-phase AC from the grid (50 Hz, 400 V) to DC, and the PMSM-side converter generates the required three-phase AC with the desired voltage and frequency for the PMSM. In off-grid mode, with a battery as the power source, only one converter is needed to provide AC current to the PMSM during start-up. In generation mode, the grid-side converter can be used depending on the consumer's AC or DC current requirements.

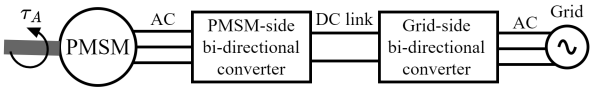

Figure 4. Schematic of the electrical system components and their arrangement in the motoring mode (grid-connected).

4.1. PMSM

PMSM control is complicated due to its three-phase AC current. To simplify control, a Park–Clark transformation converts three-phase variables into a two-dimensional coordinate system (d-q frame) using DC values, aligning with classical linear control theory [52]. The equations below describe the PMSM mathematical model with DC-transformed parameters.

$$\frac{dI_q}{dt} = \frac{1}{L_q}[V_q - R_s I_q - L_d \omega_e I_d - \phi_{mg} \omega_e] \quad (36)$$

$$\frac{dI_d}{dt} = \frac{1}{L_q}[V_d - R_s I_d + L_q \omega_e I_q] \quad (37)$$

$$\tau_A = 3 Z_P [\phi_{mg} I_q + (L_q - L_d) I_q I_d] \quad (38)$$

where I_q, I_d, V_q, V_d, R_s, L_q, L_d, ϕ_{mg}, ω_e, τ_A and Z_p are q-axis current, d-axis current, q-axis voltage, d-axis voltage, the resistance of PMSM stator, q-axis inductance, d-axis inductance, flux induced by the permanent magnets of the rotor, electromagnetic speed, electromagnetic torque and pole pairs of the PMSM. The electromagnetic speed is calculated as follows:

$$\omega_e = \omega_m Z_p. \quad (39)$$

where ω_m is the mechanical rotational speed of the shaft.

In this study, the PMSM model is simplified by assuming negligible dynamics in PMSM current (dI_q/dt and dI_ddt are set to zero). This is reasonable, as electric current dynamics are much faster than shaft dynamics. Consequently, the equations for RMS voltage, RMS current, and PMSM power are as follows. The I_d component, which does not generate torque, is typically controlled to be 0 which is coming from the field-oriented control strategy [52]. RMS values represent the effective equivalent of varying voltage or current, derived from mean squared values over an interval.

$$I_q = \frac{1}{3Z_p}\frac{\tau_A}{\phi_{mg}} \tag{40}$$

$$I_d = 0 \tag{41}$$

$$V_d = -L\omega_e I_q \tag{42}$$

$$V_q = R_s I_q + \phi_{mg}\omega_e \tag{43}$$

$$I_{RMS} = \sqrt{I_q^2 + I_d^2} \tag{44}$$

$$V_{RMS} = \sqrt{V_q^2 + V_d^2} \tag{45}$$

$$PW_A = \omega_m \tau_A \tag{46}$$

The calculated electric power is what the PMSM provides to the MGT during start-up. Yet, the power source needed for the PMSM is higher, accounting for PMSM power losses. Two main losses have been considered in this study. One is the copper loss coming from stator resistance. The other loss is accounted for by additional losses that is calculated by using a coefficient of speed [17]. Thus, the electric power source required for PMSM feeding voltage is calculated accordingly.

$$PW_e = \frac{3}{2}V_q I_q + K_{HSA}N \tag{47}$$

in which PW_e, K_{HSA}, and N are the electric power required for the PMSM, HSA multiplier for additional losses provided by the manufacturer, and shaft speed in rpm.

4.2. Bi-Directional Converter

A bi-directional converter, utilising insulated-gate bipolar transistors (IGBTs), transforms DC to three-phase AC for the PMSM. This process incorporates Pulse Width Modulation (PWM) to generate variable-width pulses, simulating continuous voltage [52]. Typically, six IGBTs handle three-phase currents that cause power losses in addition to transforming AC/DC or DC/AC, encompassing conduction and switching losses [53]. This power loss leads to finding the necessary power input for the bi-directional converter.

$$PW_{cvt} = PW_e + PW_{cvt,loss} \tag{48}$$

where cvt refers to the bi-directional converter and PW_{cvt} is the power of the current to be fed to the converter. The power loss of the converter, denoted as $PW_{cvt,loss}$, consists of two components: conduction and switching power loss.

When the IGBT carries current in its on-state, it behaves like a series of components: a resistor and a DC voltage source. The equivalent circuit is shown in Figure 5. Power losses occur in both the resistor and DC source, contributing to IGBT conduction losses. The zero current voltage $V_{0,I}$ can be obtained from the IGBT datasheet [54].

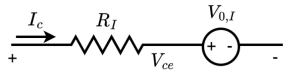

Figure 5. Equivalent circuit of an IGBT for on-state condition.

Based on the equivalent circuit shown in the figure, the conduction power loss is calculated by Equation (49) [53]:

$$PW_{cond} = {I_{RMS}}^2.R_I + V_{0,I}.I_{avg} \tag{49}$$

where R_I is the resistance of the IGBT on collector–emitter current (on-state resistance) and I_{avg} is the average current that is calculated by using RMS current ($I_{avg} = 2.\sqrt{2}.I_{RMS}$). The subscript of *cond* stands for conduction loss.

Since IGBTS are switching devices, some of the energy is lost during switching on and off. The values for E_{on} and E_{off}, which are the energy loss for switching on and off respectively, are provided by the manufacturer in the datasheet for IGBT energy losses in specific test conditions. However, test conditions differ from actual operating conditions. According to [55], E_{on} and E_{off} are proportional to the current through IGBT in on-state conditions and voltage in off-state conditions. Therefore the actual energy losses are estimated based on Equations (50) and (51) [53] using on-state current and off-state voltage:

$$E_{on,I} = \frac{\sqrt{2}}{\pi}.\frac{V_{DC}}{V_{ce,ref}}.\frac{I_{RMS}}{I_{c,ref}}.E_{on,ref} \tag{50}$$

$$E_{off,I} = \frac{\sqrt{2}}{\pi}.\frac{V_{DC}}{V_{ce,ref}}.\frac{I_{RMS}}{I_{c,ref}}.E_{off,ref} \tag{51}$$

where the subscripts of *DC* and *ref* refer to *DC* voltage source and reference value respectively.

The calculated energy is for a duty cycle of PWM. In order to find out the power loss of the switching devices, the calculated energy should be multiplied by the frequency of the switching:

$$PW_{sw} = (E_{on,I} + E_{off,I}).f_{sw} \tag{52}$$

where PW_{sw} and f_{sw} are the switching loss and switching frequency.

5. Control System

The controlled parameter in CSP-MGTs, shaft speed, utilises a Proportional-Integral (PI) controller. Design coefficients, proportional gain (k_p) and integral gain (k_I) require determination for controller design via system transfer function derivation.

To derive the system's transfer function, the governing equations should be extracted. Figure 6 depicts speed as the controlled parameter and torque as the controlling parameter. Although PMSM voltage is ideal, this study does not consider voltage and current dynamics, using a steady-state model for calculation. Consequently, torque becomes the controlling parameter instead of voltage.

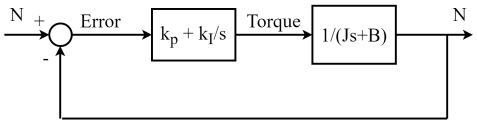

Figure 6. Closed-loop of the system with the transfer function and PI controller.

The CSP-MGT system has six primary transient sources: heat soakage in the compressor and turbine, the recuperator and solar receiver, mass imbalances, and shaft speed. The differential equation for shaft speed (Equation (32)) is used for the transfer function, with τ_A termed τ_g. Torque loss is estimated as a linear function of shaft speed ($B\omega$), where B is viscosity friction and it is derived from Equation (35). Laplace transformation of Equation (32) shifts the equations to the frequency domain.

$$Js\omega = \tau_t(s) - \tau_c(s) - \tau_A(s) - B\omega \tag{53}$$

$$\tau_t - \tau_c - \tau_A(s) = \tau_g \tag{54}$$

$$\frac{\omega}{\tau_g} = \frac{1}{Js + B} \tag{55}$$

The PI controller function in the frequency domain is as follows:

$$k_p + \frac{k_I}{s} \tag{56}$$

Therefore, the closed-loop becomes as follows.

As it can be observed from Figure 6, the open-loop function of the system is $1/Js + B$. Based on the general form of the function of the first-order systems which is $C/1 + \tau s$ (where C is a constant value and τ is the time constant), it can be deduced that $\tau = B/J$.

By using the closed-loop system shown in Figure 6, the whole system transfer function with the controller can be written as below:

$$\frac{Output}{Input} = \frac{k_p s + k_I}{Js^2 + (k_p + B)s + k_I} \tag{57}$$

With the help of the standard form of the second-order equations which has a denominator of $s^2 + 2\zeta\omega_n + (\omega_n)^2$, the two coefficients of the PI controller are found. The values for the PI controller coefficients are provided in the next sections.

6. Simulation Process

Figure 7 illustrates the overall structure of the coupled electro-thermo-mechanical CSP–MGT model, highlighting the interactions between the thermodynamic components, shaft dynamics, electrical system, and control architecture.

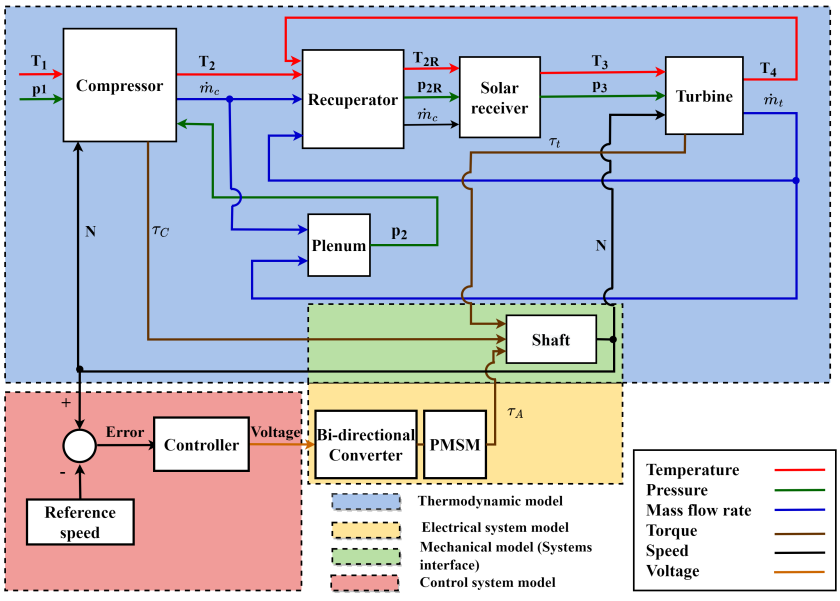

Figure 7. The layout of the developed electro-thermo-mechanical model in MATLAB/Simulink.

This study primarily focuses on simulating the off-grid operation of the CSP-MGT during its start-up phase. To simulate this scenario, it is assumed that the battery is the primary power source, supplying DC electric current during the system's start-up phase. The electric power calculated at each time step represents the power required for the bi-directional converter positioned before the PMSM. The transient model of the entire CSP-MGT system comprises a set of ordinary differential equations, resulting from the modelling of each subsystem. Specifically, there is one equation for the compressor, one for the turbine, five for the recuperator, seven for the solar receiver, one for the shaft, and one for the plenum. Five primary state variables are considered: $T_{m,c}$, $T_{m,t}$, $T_{m,recu}$, $T_{m,recv}$, p_2, and N. Among these variables, $T_{m,recu}$ and $T_{m,recv}$ represent composite variables with five and seven temperatures, respectively, as they describe the one-dimensional models of the recuperator and solar receiver. The initial values of these state variables depend on the system's initial conditions, determined by the type of start-up, whether cold or warm. The model receives inputs from two sources: ambient conditions and PMSM voltage. The PMSM voltage is sourced from the bi-directional converter, which receives it from the assumed battery. The voltage value is determined by the controller. Once the initial conditions and inputs are established, the simulation commences with calculations starting from the compressor, following a predefined sequence. At each time step, the six state variables are updated based on computations within each model component. To determine the new value of the N state variable, the required torque by the compressor (τ_c), the generated torque by the turbine (τ_t), and the mechanical torque loss (τ_{loss}) are added to the torque from the PMSM (τ_A). Solving the resulting differential equation yields the updated value of the state variable of N. The speed feedback signal is then relayed to the controller, which generates the necessary PMSM voltage to produce the τ_A torque.

7. Results and Discussion

7.1. Model Validation

To evaluate the model, validation and verification are conducted in two stages. First, individual components are validated using available experimental data, focusing on transient behaviour. Second, all the CSP-MGT model results are compared with the experimental measurements to consider the interactions of the components. The experimental data are for a 6 kW_e CSP-MGT which was tested at the ENEA (Italian National Agency for New Technologies, Energy and Sustainable Economic Development) Casaccia site for the OMSoP project. The design parameters of this system are listed in Table 1. However, the available measurements from this test are for the motoring mode, and not for the generation mode.

Table 1. Design parameters of 6 kW_e CSP-MGT of OMSoP project [56–58].

Parameter	Value
DNI [W/m^2]	800
N [krpm]	130
TIT [K]	1073
TOT [K]	923
Power output [kW_e]	6
Compressor pressure ratio [-]	3
Air mass flow rate [kg/s]	0.088

The key model parameters and material properties used in the simulations are summarised in Tables 2–4. These parameters include thermo-mechanical properties of the main components, solar dish characteristics, and electrical and shaft parameters.

Table 2. Thermo-mechanical component parameters used in the transient model.

Component	Parameter	Value
Compressor	Metal mass M_c [kg]	1.38
	Heat capacity C_c [J/(kg·K)]	900 [59]
Turbine	Metal mass M_t [kg]	2.15
	Heat capacity C_t [J/(kg·K)]	Temperature-dependent $C(T)$ from [60]
Recuperator	Metal mass M_{recu} [kg]	50
	Heat capacity C_{recu} [J/(kg·K)]	Temperature-dependent $C(T)$ from [60]
Receiver	Metal mass M_{recv} [kg]	20
	Nozzle diameter d [m]	0.01
	Number of nozzles n_{nozzle} [-]	12
	Heat capacity C_{recv} [J/(kg·K)]	Temperature-dependent $C(T)$ from [60]

Table 3. Solar dish parameters.

Parameter	Value
Dish area A_{dish} [m^2]	88
Optical efficiency η_{opt} [-]	0.409

Table 4. Electrical machine and shaft parameters.

Component	Parameter	Value
PMSM	Pole pairs Z_p [-]	2
	L_d, L_q [mH]	0.316
	Flux linkage ϕ_{mg} [Wb]	0.01153
Shaft	Inertia J [kg·m^2]	1.1×10^{-4}

7.1.1. Turbomachinery Components

As previously mentioned, the low-speed curves for turbomachinery components are generated by interpolating existing curves, employing a zero-speed line for the compressor and a zero-speed point for the turbine. However, this mathematical approach requires calibration with experimental data. Each speed curve encompasses various operating points with differing pressure ratios and modified mass flow rates. Ideally, multiple measurements per speed curve would ensure accurate calibration, but often only one operating point per curve is available and this is also the case for this study. These speed curves are calibrated using experimental data from City, University of London, gathered from tests on a 6 kW_e MGT in the laboratory. This has to be noted that since the MGT was designed to operate mostly at the design point and not low speeds that are far from the design points, the measurements were exposed to higher measurement uncertainty compared to the points close to design conditions.

Tuning the Generated Map

To adjust the generated map at lower speeds according to the measured data, the position of the speed lines was modified slightly, while maintaining their shape, until they matched the measured data while considering the relative uncertainty according to the measurements [57]. The interpolation and curve fitting were performed using polynomial β-lines.The tuning results for the compressor and turbine maps can be observed in Figures 8 and 9, respectively. It is evident from the figures that the generated speed curves pass through the operating points or the uncertainty zones.

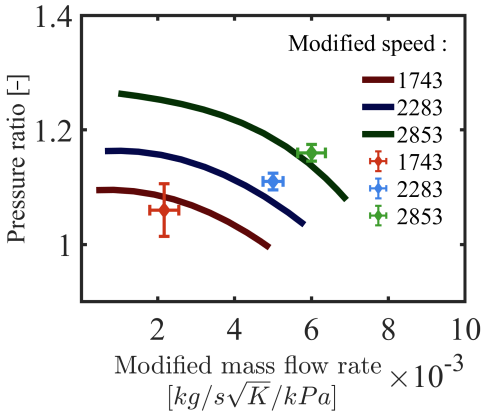

Figure 8. Tuning of the generated map for the low-speed curves of the compressor with the measured data.

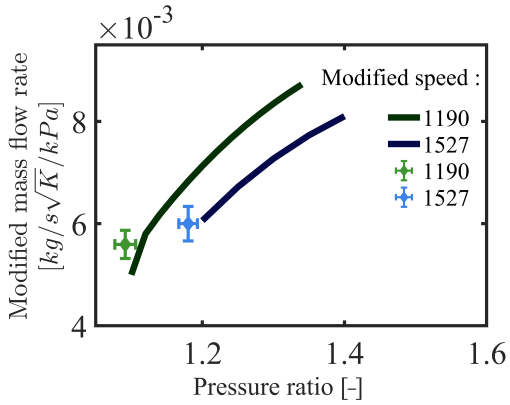

Figure 9. Tuning of the generated map for the low-speed curves of the turbine with the measured data.

Once the generated performance map has been tuned with the actual steady-state operating points for the low-speed region, it is necessary to confirm the validity of the interpolation methodology for all operating ranges of the performance map. For this purpose, the performance map of the Turbec T100PH Series as reported by the German Aerospace Center (DLR) was used [61]. The validation results are shown in Table 5. Since the experimental data were only available for the compressor, the validation was only done for the compressor. The parameters of validations were chosen to be the air mass flow rate and the steady-state compressor outlet temperature.

Table 5. The validation of the model of the turbomachinery components for steady-state values.

Parameter	Relative Error
Compressor air mass flow rate	<6 %
Compressor outlet temperature	<3.2 %

As illustrated in Table 5, this validation shows that the linear interpolation methodology could be used in this study for the following stages.

7.1.2. Recuperator

The initial validation of the recuperator focused on the Colburn and friction factors, utilising experimental data. This validation process was applied to a plate-fin heat exchanger with dimensions of 1/10-27.03 as detailed in a study by [45], with the geometric specifications, sourced from Kays and London's work, Figure 10 [62].

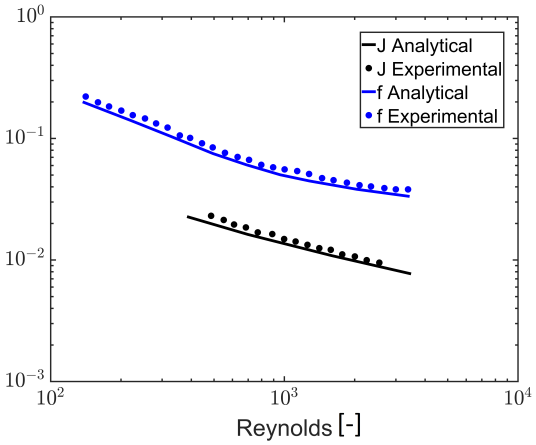

Figure 10. Variation in Colburn and friction factors with Reynolds number [43].

This result ensures that the heat transfer coefficients used in the energy conservation equation and the friction factor used in calculating the pressure drop are in agreement with experimental data. The comparison between the model predictions and experimental data for the Colburn factor j and friction factor f is shown as a function of Reynolds number. The model replicates the experimental trends accurately across the full range, including the low Reynolds number regime corresponding to low mass flow rates. The maximum relative deviation is about 3% [43]. This demonstrates that the model's sensitivity to variations in the heat transfer coefficient is small, even at low flow conditions, and confirms the robustness of the predicted recuperator performance.

Additionally, thermal validation of the recuperator was performed by comparing the predicted outlet temperatures with experimental measurements. Accordingly, a dedicated recuperator model layout was defined, as shown in Figure 11. To assess the sensitivity of the one-dimensional recuperator model to spatial discretisation, the number of discretised cells was increased from three to seven, and the resulting outlet temperatures were evaluated. It was observed that increasing the number of cells beyond five did not lead to a noticeable change in the predicted outlet temperature. Based on this observation, five discretised cells were selected as a compromise between numerical accuracy and computational efficiency. The inputs to the model are the measured hot- and cold-side inlet air temperatures and mass flow rates, while the predicted hot- and cold-side outlet air temperatures are compared against their experimental counterparts, Figure 12.

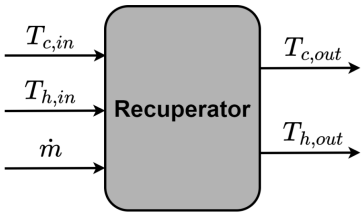

Figure 11. The layout of the recuperator component for the thermal model.

The results show a maximum deviation of 4.6% and 4.7% for hot- and cold-side outlet air temperatures, respectively, compared to experimental values. The temperature trend is generally well-replicated, but an initial deviation is likely due to sudden air mass flow rate changes and possible measurement uncertainties at low flow rates. Model inaccuracies may also result from limited initial recuperator metal temperature data.

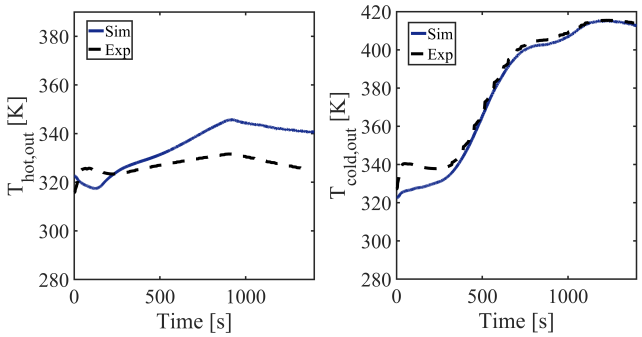

Figure 12. Validation results of the recuperator thermal model.

7.1.3. Solar Receiver

The approach used to validate the thermal model of the solar receiver follows the same methodology adopted for the recuperator. In addition, the discretisation of the receiver into a finite number of cells is similar with the approach used for the recuperator. Therefore, the same validation strategy was applied to this component. The layout of the thermal model of the solar receiver is shown in Figure 13.

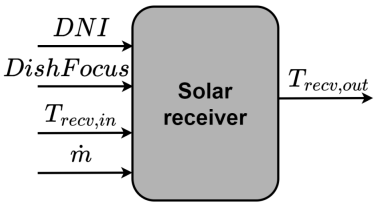

Figure 13. The layout of the thermal model of solar receiver component in the transient model.

The solar receiver thermal model has four inputs: DNI, dish focus schedule, receiver inlet air temperature ($T_{recv,in}$) and mass flow rate ($\dot{m}$). The dish focus schedule determines focused and unfocused periods based on sun and dish azimuth angles, where unfocused periods were due to practical limits during tests to prevent turbine bearing overheating (see Figure 14 for the solar receiver's focusing schedule).

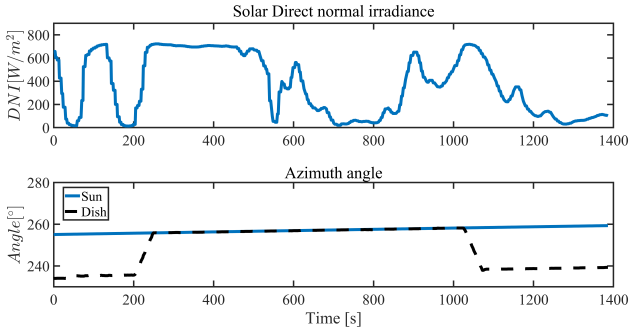

Figure 14. DNI and dish focusing schedule for the receiver thermal model.

Using the inputs given to the solar receiver model, the outlet air temperature of the receiver is found. The results of the model and the corresponding experimental measurements are presented in Figure 15 for comparison. The validation of the solar receiver model focused solely on its thermal aspects since the validation of pressure drop has been already provided in [46].

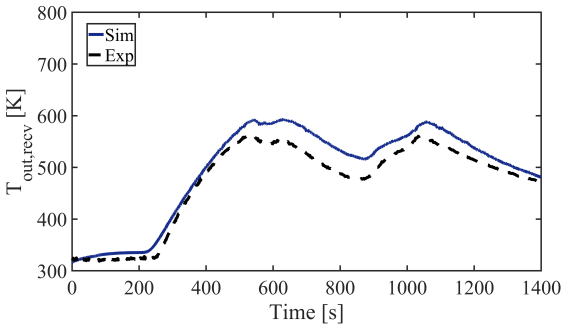

Figure 15. Validation results of the solar receiver thermal model.

As depicted in Figure 15, the maximum deviation of the solar receiver's outlet air temperature is approximately 8%, indicating a relatively high level of error. One of the main reasons for this deviation is the underestimation of receiver heat loss. The model's convective/radiative loss terms depend strongly on assumed correlations, emissivity, effective loss area, and boundary conditions. Another reason is due to heat transfer modelling simplifications inside the receiver. Since the impinging-jet local correlation near stagnation with Dittus–Boelter elsewhere were mixed, and the receiver was discretised into 1D cells, there could be a mismatch between real flow distribution and the assumed correlation regions.

It should be noted, however, that due to limited access to the experimental plant, a comprehensive understanding of the system's components was not possible.

7.1.4. PMSM and Bi-Directional Converter

Since the experimental data for electrical current was not available, validation of the PMSM was done at the design conditions where power is 6 kW_e and 130 krpm with electric torque of 0.44 at RMS voltage/current of 170 V/13 A. The RMS current is linearly proportional to the electric torque which is linked to the compressor/turbine inlet and outlet temperatures and air mass flow rate. Therefore, validated temperatures ensure precise electric current prediction. RMS voltage, on the other hand is tied to speed which was verified at 170 V [63] by calculating the voltage value of PMSM. This yielded 168.1 V, with a 1% deviation. PMSM efficiency at nominal conditions was also calculated with less than 1% difference from the reference value.

The selection of an IGBT converter is crucial in determining its performance in a given operating condition. The main parameters that are considered when selecting an IGBT converter include its nominal voltage and electric current ratings. As mentioned earlier, a six IGBT topology has been chosen for this study. This ensures a stable and efficient power transfer, making it a popular choice for many applications. Based on the datasheet from [54], the chosen IGBT for the study was selected to ensure its suitability for the intended application. It has to be noted that since the bi-directional converter operates in both motoring and generation conditions, the efficiency in the two operating modes is different. This is due to the dependency of the power loss on the upstream voltage. This means that when the converter is working in the motoring mode, the DC link voltage is used in Equations (50) and (51) and when it is working in the generation mode, the RMS voltage of the three-phase voltage after the generator is used. The assumed switching frequency for calculating the IGBTs' switching losses is determined to be 16 kHz based on experimental data.

7.1.5. Control System Design

Designing the controller can be done by considering the system's transfer function. For the transfer function as a second-order equation, damping ratio (ζ) and natural frequency

(ω) define system behaviour, enabling controller coefficient determination, as depicted in Table 6.

Table 6. Coefficients of the designed PI controller.

Coefficient	Value
k_p	8.4×10^{-5}
k_I	4×10^{-4}

7.1.6. CSP-MGT System

After validating each subsystem using experimental measurements and defining the parameters of the control model, validation of the entire CSP–MGT system is required to ensure that the full transient behaviour is captured accurately. Integrating all components allows their thermal, mechanical, and electrical interactions to be represented, enabling evaluation of system dynamics beyond what isolated component tests can show. For system-level validation, the complete transient model is provided with the same input conditions used during testing, including ambient temperature, ambient pressure, DNI and the implemented dish focusing schedule, as illustrated in Figure 16. The resulting outputs of the model—TIT, TOT, compressor outlet temperature (COT), air mass flow rate, compressor pressure ratio and turbine pressure ratio—are compared directly with the corresponding experimental measurements, presented in Figure 17.

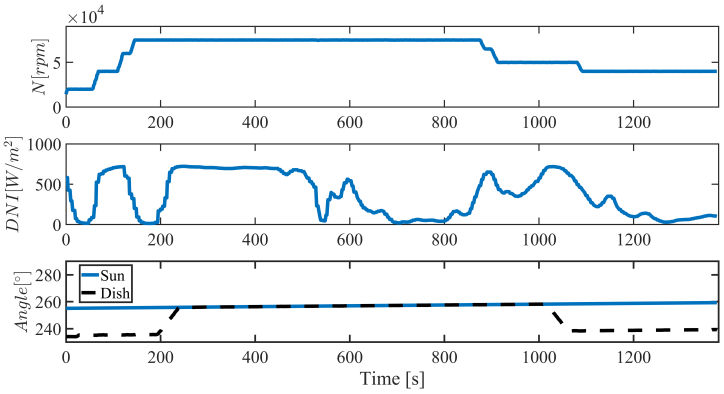

Figure 16. The inputs of the CSP-MGT system model for validation.

As discussed previously in the solar receiver section, continuous full-focus operation of the dish was not possible due to the risk of bearing overheating. Instead, a focusing schedule was applied to intermittently reduce the concentration at the receiver. This schedule was not optimised and was selected based on operator feedback to maintain thermal safety during testing. By applying the same input conditions to the model, the transient outputs can be compared fairly against experimental results.

Figure 17 demonstrates a strong agreement between simulation and experiment, confirming that the transient behaviour of the CSP–MGT system is well-represented. The predicted COT shows a maximum deviation of 4%, reflecting an accurate reproduction of the thermal trend influenced by isentropic efficiency, pressure ratio, ambient conditions and heat soakage. TIT and TOT differ from the measurements by up to 8%, which is acceptable for transient receiver operation and consistent with the observations made during component-level validation. The largest discrepancy appears in air mass flow rate, which is expected due to the high measurement uncertainty during testing and the fact that the system was originally designed for steady-state rather than transient operation. Compressor and turbine pressure ratios show a maximum deviation of 7% and follow the experimental trends closely throughout the transient cycle.

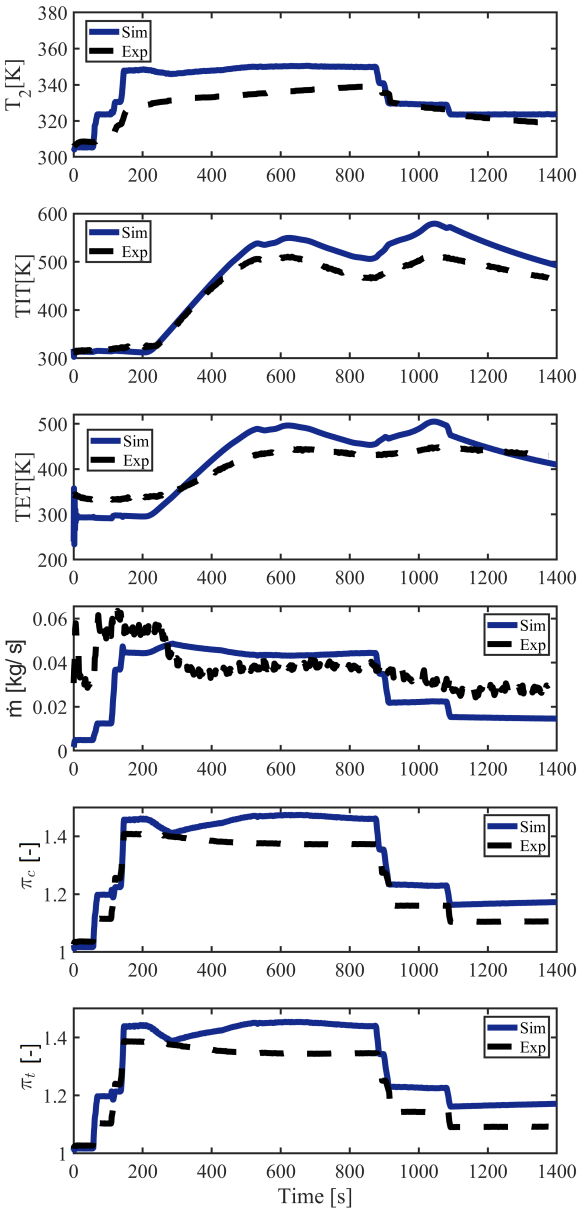

Figure 17. Validation results of the CSP-MGT system model.

The results confirm that the developed transient model accurately captures the dynamic response of the CSP–MGT system at both the component and system levels. Although validation was performed during the start-up phase, the model remains applicable to power generation, as the start-up phase represents the most demanding operating regime, requiring accurate representation of heat soakage effects and coupled thermo-mechanical–electrical behaviour. The uncertainty associated with the experimental measurements was estimated based on manufacturer-specified instrument accuracies and was considered when interpreting the validation results. It should be noted that a substantial portion of the validation data corresponds to off-design operating conditions, particularly during start-up and low-speed operation. Under these conditions, measurement uncertainty increases and the system response becomes highly sensitive to small variations in mass flow rate and temperature, such that relatively small absolute measurement errors can result in larger relative deviations between the simulation and experimental results.

7.2. Start-Up Transients with Heat Soakage

Another contribution of this study lies in the explicit inclusion of heat soakage in the metal components of the MGT. Unlike off-design models, which assume an instantaneous thermal response, the present model accounts for the thermal mass and conductive heat absorption of the metals, giving it genuine transient fidelity. This feature is particularly critical during start-up, when steep changes in DNI and shaft speed occur, and turbine metal temperatures evolve dynamically rather than immediately.

In addition, the bi-directional coupling between the electrical and thermo-mechanical sub-models enables assessment of how thermal transients influence shaft power production, and, conversely, how electrical load affects thermal state. To illustrate this, two simulations were performed using the same speed schedule and DNI profile from the OMSoP validation dataset: one including heat soakage and one with component mass removed. The results are presented in Figures 18 and 19.

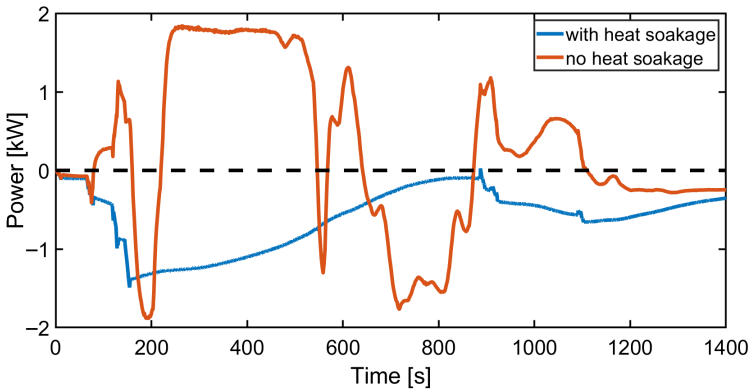

Figure 18. Comparison of electrical power for the effect of considering heat soakage in the transient model. The black dashed line shows zero power line.

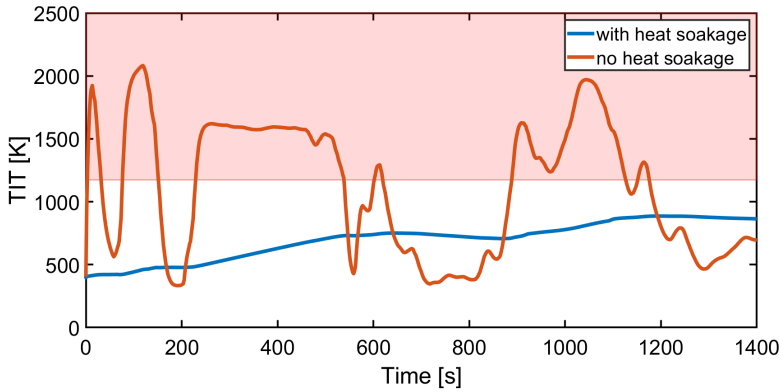

Figure 19. Comparison of turbine inlet temperature for the effect of considering heat soakage in the transient model. The red shadow area shows the out-of-safety-limit temperature.

Figure 18 shows that when heat soakage is neglected, electrical power responds almost instantaneously to DNI fluctuations. In this artificial case the power trace closely mirrors the irradiance input, and during the interval from 200–600 s, where both shaft speed (~80 krpm) and DNI (~700 W/m²) remain steady, the system produces nearly 1.8 kW of electrical power. This behaviour does not appear in the physically representative case including heat soakage, where no power generation occurs—consistent with experimental observation—demonstrating that thermal inertia strongly suppresses power recovery during start-up.

The underlying mechanism is clarified in Figure 19, where the turbine inlet temperature (TIT) rises sharply without heat soakage, tracking DNI with minimal lag. The shaded

region highlights temperatures exceeding the material limit, indicating that neglecting heat absorption by the metal structure leads to unrealistically high TIT transients. In contrast, when heat soakage is included, TIT evolves gradually and remains within acceptable limits throughout the cycle.

The results show that exclusion of heat soakage leads to a superficial decrease of up to 140% in the estimated electrical energy consumption during the start-up phase. This effect is attributed to the small scale of the micro gas turbine, for which thermal mass effects are significantly more influential than in larger gas turbines, where corresponding deviations are typically of the order of 30% [30].

These findings emphasise that an off-design, steady-state thermal representation is insufficient for start-up analysis. The transient soakage behaviour is a dominant driver of both temperature evolution and shaft power capability, meaning that start-up optimisation, component life prediction, and thermal–electrical control strategies cannot be reliably evaluated without a fully transient heat soakage-aware model.

8. Conclusions

In this study, the development of a transient model for a CSP-MGT comprising of thermo-mechanical and electrical models was presented in detail. The thermo-mechanical part of the model is based on a lumped-volume and one-dimensional discretisation approach which is capable of simulating the transient performance of the system in response to the intermittent nature of the input thermal power. Thermodynamics, heat transfer to the casing and surroundings, shaft rotation, electrical system, control system dynamics as well as mass and heat storage are simulated together to account for their interactions. The model can also be used for real-time simulations due to having three hundred times less simulation time than the real transient process. Furthermore, the following points can be concluded from the results presented in this study.

- A transient electro-thermo-mechanical model was developed for the start-up phase of CSP-MGT. The model has the capability of modelling electrical components which gives an insight into the electrical current and electrical power dynamics affected by the thermal and mechanical dynamics in the the CSP-MGT system.
- A transient model was validated for individual components and the entire CSP-MGT system. At the component level, the solar receiver outlet temperature showed the highest validation error (8% error). At the system level, validation revealed significant deviation in predicted air mass flow rate due to measurement inaccuracies at lower speeds.
- The comparison between the transient simulations with and without heat soakage demonstrated that neglecting thermal inertia leads to unrealistic, instantaneous temperature response to DNI, emphasising the importance of including heat soakage in the model.

The developed model has the potential to be applied in diverse analyses concerning various operations of the CSP-MGT. With its incorporation of an electrical system model, it has the capacity to offer transient insights into both electrical and thermo-mechanical parameters. This model is aimed to be used for the optimisation of the start-up phase of CSP-MGT in future study.

Author Contributions: Conceptualization, J.A.-Z. and S.S.A.; Methodology, S.S.A. and J.A.-Z.; Software, S.S.A.; Data curation, J.A.-Z.; Investigation, J.A.-Z. and S.S.A.; Writing—original draft, S.S.A.; Writing—review and editing, J.A.-Z. and A.I.S.; Visualization, S.S.A.; Supervision, J.A.-Z. and A.I.S. All authors have read and agreed to the published version of the manuscript.

Funding: This research received no external funding.

Data Availability Statement: The original contributions presented in this study are included in the article. Further inquiries can be directed to the corresponding author.

Conflicts of Interest: The authors declare no conflicts of interest.

Abbreviations

CFD	Computational fluid dynamics
CSP	Concentrated solar power
DNI	Direct Nominal Irradiance
HSA	High-speed alternator
ICMF	Iterative constant mass flow
ICV	Inter-component volume
IGBT	Insulated-gate bipolar transistor
MGT	Micro gas turbine
PMSM	Permanent magnet synchronous machine
OMSoP	Optimised Microturbine Solar Power system
PV	Photovoltaic

Symbols

A	Heat transfer area [m^2]
A_1	Minimum free-flow area of fluid 1 [m^2]
B	Viscous friction factor [N.m/rad/s]
C	Specific heat capacity of metal [kJ/(kg·K)]
c_p	Specific heat capacity [kJ/(kg·K)]
d	Nozzle diameter of the receiver [m]
D	Pitch circle diameter of the bearing [m]
D_c	Hydraulic diameter of the equivalent duct of the compressor [m]
D_h	Hydraulic diameter of the equivalent duct of one side of the heat exchanger [m]
$E_{on,I}$	IGBT energy loss during switching on [J]
$E_{off,I}$	IGBT energy loss during switching off [J]
f	Fanning friction factor [-]
f_{sw}	Switching frequency [kHz]
G	Fluid mass velocity [kg/(s.m^2)]
I_d	d-axis electric current [Amps]
I_q	q-axis electric current [Amps]
j	Colburn number [-]
J	Rotational mechanical inertia of the shaft [kg·m^2]
k_{air}	Thermal conductivity of air [kW/(m.K)]
K_{HSA}	Multiplier for calculating iron losses of motor [V/krpm]
k_I	Integral coefficient of the controller [-]
k_p	Proportional coefficient of the controller [-]
L	Airflow length on one side of the heat exchanger [m]
L_d	d-axis inductance [H]
L_q	q-axis inductance [H]
$\dot{m}$	Mass flow rate [kg/m^2]
M	Metal mass [kJ/(kg·K)]
N	Shaft speed [rpm]
Nu	Nusselt number [-]
n	Number of cells for one-dimensional model [-]
n_{nozzle}	Number of nozzles on receiver [-]
p	Pressure [kPa]

PW	Power [kW]
PW_{sw}	Switching power loss [kW]
Pr	Prandtl number [-]
Q	Heat transfer rate [kW]
R	Gas constant [J/(kg·K)]
Re	Reynolds number [-]
t	Time [s]
U	Heat transfer coefficient [kW/(m^2.K)]
h_x	Heat transfer coefficient at distance x from stagnation point [kW/(m^2.K)]
$V_{0,I}$	Voltage of IGBT at zero current [Volts]
V_c	Collector voltage [Volts]
V_{ce}	Collector–emitter voltage [Volts]
V_{jet}	Air jet velocity [m/s]
V_{plenum}	Plenum volume [m^3]
V_d	d-axis voltage [Volts]
V_q	q-axis voltage [Volts]
Z_p	Pole pairs of PMSM [-]

Greek letters

π	pressure ratio [-]
ρ	density [kg/m^3]
η	Efficiency [-]
γ	Specific heat ratio [-]
ϕ_{mg}	Flux linkage induced by the motor [Wb]
ζ	Damping ratio [-]
Δ	Difference
μ	Dynamic viscosity [kg/(m.s)]
τ	Torque [N.m]
ω	Shaft speed [rad/s]

Subscripts

1	Compressor inlet
2	Compressor outlet
$2, ss$	Steady-state compressor outlet
3	Turbine inlet
4	Turbine outlet
$4, ss$	Steady-state turbine outlet
A	High speed alternator
abs, i	absorbed for receiver's ith cell
a, c	compressor air
amb	Ambient
a, t	turbine air
c	compressor
$conv, loss$	Receiver convection loss
$cvt, loss$	Converter loss
e	electric
eff	effective
m, c	compressor metal
m, t	turbine metal
mf	modified
$m, recu$	recuperator metal
$m, recv$	receiver metal

opt	optical
$rad, loss$	Receiver radiation loss
$recu$	recuperator
$recv$	Receiver
$recv, in$	Receiver inlet
$recv, out$	Receiver outlet
ref	Reference
RMS	Root mean square
st	Stagnation point
t	turbine
t, ss	Steady-state parameter of turbine

References

1. European Commission. *Going Climate-Neutral by 2050: A Strategic Long-Term Vision for a Prosperous, Modern, Competitive and Climate-Neutral EU Economy*; Publications Office of the European Union: Luxembourg, 2019.
2. Küfeoğlu, S. SDG-7 Affordable and Clean Energy. In *Emerging Technologies: Value Creation for Sustainable Development*; Springer: Cham, Switzerland, 2022; pp. 305–330.
3. Voropai, N.; Stennikov, V.; Senderov, S.; Barakhtenko, E.; Voitov, O.; Ustinov, A. Modeling of integrated energy supply systems: Main principles, model, and applications. *J. Energy Eng.* **2017**, *143*, 04017011. [CrossRef]
4. Ji, Z.; Yu, X.; Li, W.; Niu, D. A multi-criteria decision-making framework for distributed generation projects investment considering the risk of electricity market trading. *J. Clean. Prod.* **2023**, *416*, 137837. [CrossRef]
5. Furlan, G.; You, F. Robust design of hybrid solar power systems: Sustainable integration of concentrated solar power and photovoltaic technologies. *Adv. Appl. Energy* **2024**, *13*, 100164. [CrossRef]
6. Orangzeb, S.; Qaisrani, M.A.; Shafiq, M.B.; Ahmed, N.; Sahar, M.S.U.; Ullah, S.; Farooq, M.U.; Jiabin, F. Potential Assessment and Economic Analysis of Concentrated Solar Power against Solar Photovoltaic Technology. *Int. J. Energy Res.* **2023**, *2023*, 3611318. [CrossRef]
7. Stengler, J.; Bülow, M.; Pitz-Paal, R. Concentrating solar technologies for low-carbon energy. *Nat. Rev. Clean Technol.* **2025**, *1*, 719–733. [CrossRef]
8. Merchan, R.P.; Santos, M.J.; Medina, A.; Calvo Hernández, A. On-and off-design thermodynamic analysis of a hybrid polar solar thermal tower power plant. *Int. J. Energy Res.* **2021**, *45*, 1789–1805. [CrossRef]
9. Kee, Z.; Wang, Y.; Pye, J.; Rahbari, A. Small-scale concentrated solar power system with thermal energy storage: System-level modelling and techno-economic optimisation. *Energy Convers. Manag.* **2023**, *294*, 117551. [CrossRef]
10. Mohammadi, A.; Mehrpooya, M. Exergy analysis and optimization of an integrated micro gas turbine, compressed air energy storage and solar dish collector process. *J. Clean. Prod.* **2016**, *139*, 372–383. [CrossRef]
11. Aboelmaaref, M.M.; Zayed, M.E.; Zhao, J.; Li, W.; Askalany, A.A.; Ahmed, M.S.; Ali, E.S. Hybrid solar desalination systems driven by parabolic trough and parabolic dish CSP technologies: Technology categorization, thermodynamic performance and economical assessment. *Energy Convers. Manag.* **2020**, *220*, 113103. [CrossRef]
12. Mokheimer, E.M.A.; Dabwan, Y.N.; Habib, M.A. Optimal integration of solar energy with fossil fuel gas turbine cogeneration plants using three different CSP technologies in Saudi Arabia. *Appl. Energy* **2017**, *185*, 1268–1280. [CrossRef]
13. Rovense, F.; Sebastián, A.; Abbas, R.; Romero, M.; González-Aguilar, J. Performance map analysis of a solar-driven and fully unfired closed-cycle micro gas turbine. *Energy* **2023**, *263*, 125778. [CrossRef]
14. Shamekhi Amiri, S.; Al-Zaili, J.; Sayma, A.I. Development of a Dynamic Model for Simulating the Transient Behaviour of a Solar-Powered Micro Gas Turbine. In *Turbo Expo: Power for Land, Sea, and Air*; ASME: New York, NY, USA, 2022; Volume 86014, p. V004T06A001.
15. Ghavami, M.; Al-Zaili, J.; Sayma, A.I. A methodology for techno-economic and operation strategy optimisation of micro gas turbine-based solar powered dish-engine systems. *Energy* **2022**, *251*, 123873. [CrossRef]
16. OMSoP. Final Report Summary—OMSOP (Optimised Microturbine Solar Power System). FP7-ENERGY. 2013. Available online: https://cordis.europa.eu/project/id/308952/reporting (accessed on 10 December 2025).
17. Lanchi, M.; Al-Zaili, J.; Russo, V.; Falchetta, M.; Montecchi, M.; Aichmayer, L. A Quasi-Steady State Model of a Solar Parabolic Dish Micro Gas Turbine Demonstration Plant. *Energies* **2022**, *15*, 1059. [CrossRef]
18. García-Ferrero, J.; Heras, I.; Santos, M.J.; Merchán, R.P.; Medina, A.; González, A.; Calvo Hernández, A. Thermodynamic and cost analysis of a solar dish power plant in Spain hybridized with a micro-gas turbine. *Energies* **2020**, *13*, 5178. [CrossRef]

19. Arifin, M.; Rajani, A.; Atmaja, T.D. Modeling and Performance Analysis of a Parallel Solar Hybrid Micro Gas Turbine. In *Proceedings of the 2019 International Conference on Sustainable Energy Engineering and Application (ICSEEA), Tangerang, Indonesia, 23–24 October 2019*; IEEE: Jakarta, Indonesia, 2019; pp. 62–68.
20. Hashmi, M.B.; Mansouri, M.; Assadi, M. Dynamic Performance and Control Strategies of Micro Gas Turbines: State-of-the-Art Review, Methods, and Technologies. *Energy Convers. Manag. X* **2023**, 100376.
21. Kim, J.H.; Kim, T.S.; Ro, S.T. Analysis of the dynamic behaviour of regenerative gas turbines. *Proc. Inst. Mech. Eng. Part A J. Power Energy* **2001**, *215*, 339–346. [CrossRef]
22. Traverso, A. TRANSEO code for the dynamic performance simulation of micro gas turbine cycles. In *Turbo Expo: Power for Land, Sea, and Air*; ASME: New York, NY, USA, 2005; Volume 47284, pp. 45–54.
23. Davison, C.R.; Birk, A.M. Steady state and transient modeling of a micro-turbine with comparison to operating engine. In *Turbo Expo: Power for Land, Sea, and Air*; ASME: New York, NY, USA, 2004; Volume 41715, pp. 27–35.
24. Davison, C.R.; Birk, A.M. Comparison of transient modeling techniques for a micro turbine engine. In *Turbo Expo: Power for Land, Sea, and Air*; ASME: New York, NY, USA, 2006; Volume 42401, pp. 449–458.
25. Hashmi, M.B.; Lemma, T.A.; Ahsan, S.; Rahman, S. Transient behavior in variable geometry industrial gas turbines: A comprehensive overview of pertinent modeling techniques. *Entropy* **2021**, *23*, 250. [CrossRef]
26. Camporeale, S.M.; Fortunato, B.; Mastrovito, M. A modular code for real time dynamic simulation of gas turbines in Simulink. *J. Eng. Gas Turbines Power* **2006**, *128*, 506–517. [CrossRef]
27. Traverso, A. TRANSEO: A New Simulation Tool for Transient Analysis of Innovative Energy Systems. Ph.D. Thesis, University of Genoa, Genoa, Italy, 2004.
28. Lin, P.; Du, X.; Shi, Y.; Sun, X.-M. Modeling and controller design of a micro gas turbine for power generation. *ISA Trans.* **2020**, *124*, 411–426. [CrossRef]
29. Kim, J.H.; Kim, T.S. Development of a program to simulate the dynamic behavior of heavy-duty gas turbines during the entire start-up operation including very early part. *J. Mech. Sci. Technol.* **2019**, *33*, 4495–4510. [CrossRef]
30. Walsh, P.P.; Fletcher, P. *Gas Turbine Performance*; John Wiley & Sons: Hoboken, NJ, USA, 2004.
31. Howard, J. Sub-Idle Modelling of Gas Turbines: Altitude Relight and Windmilling. Ph.D. Thesis, Cranfield University, Cranfield, UK, 2007.
32. Zachos, P.K.; Aslanidou, I.; Pachidis, V.; Singh, R. A sub-idle compressor characteristic generation method with enhanced physical background. *J. Eng. Gas Turbines Power* **2011**, *133*, 8. [CrossRef]
33. Janke, C.; Bestle, D.; Becker, B. Compressor map computation based on 3D CFD analysis. *CEAS Aeronaut. J.* **2015**, *6*, 515–527. [CrossRef]
34. Tsoutsanis, E.; Meskin, N.; Benammar, M.; Khorasani, K. A component map tuning method for performance prediction and diagnostics of gas turbine compressors. *Appl. Energy* **2014**, *135*, 572–585. [CrossRef]
35. Kim, J.H.; Kim, T.S. A new approach to generate turbine map data in the sub-idle operation regime of gas turbines. *Energy* **2019**, *173*, 772–784. [CrossRef]
36. Gaitanis, A.; Contino, F.; De Paepe, W. Real Time Micro Gas Turbines Performance Assessment Tool: Comprehensive Transient Behavior Prediction With Computationally Effective Techniques. *J. Eng. Gas Turbines Power* **2023**, *145*, 031006. [CrossRef]
37. Banihabib, R.; Assadi, M. Dynamic Modelling and Simulation of a 100 kW Micro Gas Turbine Running With Blended Methane/Hydrogen Fuel. In *Turbo Expo: Power for Land, Sea, and Air*; ASME: New York, NY, USA, 2022; Volume 86052, p. V007T18A009.
38. Raggio, M.; Bellotti, D.; Ferrari, M.L. Transient Analysis of a Micro Gas Turbine With Fuel Composition Change. In *Turbo Expo: Power for Land, Sea, and Air*; ASME: New York, NY, USA, 2022; Volume 86014, p. V004T06A013.
39. Cheng, X.; Zheng, H.; Yang, Q.; Zheng, P.; Dong, W. Surrogate model-based real-time gas path fault diagnosis for gas turbines under transient conditions. *Energy* **2023**, *278*, 127944. [CrossRef]
40. Kim, J.H.; Song, T.W.; Kim, T.S.; Ro, S.T. Model development and simulation of transient behavior of heavy duty gas turbines. *J. Eng. Gas Turbines Power* **2001**, *123*, 589–594. [CrossRef]
41. Incropera, F.P.; DeWitt, D.P.; Bergman, T.L.; Lavine, A.S. *Fundamentals of Heat and Mass Transfer*; Wiley: New York, NY, USA, 1996.
42. Henke, M.; Monz, T.; Aigner, M. Introduction of a New Numerical Simulation Tool to Analyze Micro Gas Turbine Cycle Dynamics. *J. Eng. Gas Turbines Power* **2017**, *139*, 042601. [CrossRef]
43. Iaria, D.; Nipkey, H.; Al Zaili, J.; Sayma, A.I.; Assadi, M. Development and Validation of a Thermo-Economic Model for Design Optimisation and Off-Design Performance Evaluation of a Pure Solar Microturbine. *Energies* **2018**, *11*, 3199. [CrossRef]
44. Manglik, R.M.; Bergles, A.E. Heat transfer and pressure drop correlations for the rectangular offset strip fin compact heat exchanger. *Exp. Therm. Fluid Sci.* **1995**, *10*, 171–180. [CrossRef]
45. Laria, D. Techno-Economic Assessment of a Solar Dish Micro Gas Turbine System. Ph.D. Thesis, University of London, London, UK, 2020.

46. Wang, W.; Xu, H.; Laumert, B.; Strand, T. An Inverse Design Method for a Cavity Receiver Used in Solar Dish Brayton System. *Solar Energy* **2014**, *110*, 745–755. [CrossRef]
47. Strumpf, H.J.; Kotchick, D.M.; Coombs, M.G. High-temperature ceramic heat exchanger element for a solar thermal receiver. *J. Sol. Energy Eng.* **1982**, *104*, 305–309. [CrossRef]
48. Wang, W.; Laumert, B.; Xu, H.; Strand, T. Conjugate heat transfer analysis of an impinging receiver design for a dish-Brayton system. *Sol. Energy* **2015**, *119*, 298–309. [CrossRef]
49. Wu, S.-Y.; Guo, F.-H.; Xiao, L. Numerical investigation on combined natural convection and radiation heat losses in one side open cylindrical cavity with constant heat flux. *Int. J. Heat Mass Transf.* **2014**, *71*, 573–584. [CrossRef]
50. Hofmann, H.M.; Kind, M.; Martin, H. Measurements on steady state heat transfer and flow structure and new correlations for heat and mass transfer in submerged impinging jets. *Int. J. Heat Mass Transf.* **2007**, *50*, 3957–3965. [CrossRef]
51. Wang, W.; Wang, B.; Li, L.; Laumert, B.; Strand, T. The effect of the cooling nozzle arrangement to the thermal performance of a solar impinging receiver. *Sol. Energy* **2016**, *131*, 222–234. [CrossRef]
52. Pap, Z. Model Predictive Control of Electric Drives—Design, Simulation and Implementation of PMSM Torque Control. Master's Thesis, KTH Royal Institute of Technology, Stockholm, Sweden, 2018.
53. Guo, J. Modeling and Design of Inverters Using Novel Power Loss Calculation and dc-link Current/Voltage Ripple Estimation Methods and Bus Bar Analysis. Ph.D. Thesis, McMaster University, Hamilton, ON, Canada, 2017.
54. STMicroelectronics. IGBT Datasheet—Production Data of STGW20H60DF, STGWT20H60DF; 2013. Available online: https://www.st.com/content/st_com/en.html (accessed on 10 December 2025).
55. Bierhoff, M.H.; Fuchs, F.W. Semiconductor losses in voltage source and current source IGBT converters based on analytical derivation. In Proceedings of the IEEE 35th Annual Power Electronics Specialists Conference, Aachen, Germany, 20–25 June 2004.
56. OMSoP—Optimised Microturbine Solar Power System. Available online: https://etn.global/omsop/ (accessed on 10 December 2025).
57. Khader, M.A. Development of a Micro Gas Turbine for Concentrated Solar Power Applications. Ph.D. Thesis, University of London, London, UK, 2017.
58. Ghavami, M. Cycle Analysis and Optimisation of Micro Gas Turbines for Concentrated Solar Power. Ph.D. Thesis, University of London, London, UK, 2017.
59. Linstrom, P.J.; Mallard, W.G. *NIST Chemistry WebBook, NIST Standard Reference Database Number 69*; National Institute of Standards and Technology (NIST): Gaithersburg, MD, USA, 2017.
60. Zhang, Z.; Michalski, J.; Haghighat, F.; Moreau, A. *NIST Interagency/Internal Report (NISTIR) 7401*; National Institute of Standards and Technology (NIST): Gaithersburg, MD, USA, 2007.
61. Hohloch, M.; Zanger, J.; Widenhorn, A.; Aigner, M. Experimental Characterization of a Micro Gas Turbine Test Rig. *Turbo Expo Power Land Sea Air* **2010**, *43987*, 671–681.
62. Kays, W.M.; London, A.L. *Compact Heat Exchangers*; McGraw-Hill: New York, NY, USA, 1984.
63. e+a Elektromaschinen und Antriebe AG. Motor Datasheet—Motor Type mSpW 5.4/4-2-d1; 2015. Available online: https://www.eunda.ch/en/ (accessed on 10 December 2025).